9-5-2018

Tip-Enhanced Stimulated Raman Scattering with Ultra-High-Aspect-Ratio Tips and Confocal Polarization Raman Spectroscopy for Evaluation of Sidewalls in Type II Superlattices FPAs

D. A. Tenne
Boise State University

 doi: 10.1117/12.2504541

Tip-enhanced stimulated Raman scattering with ultra-high-aspect-ratio tips and confocal polarization Raman spectroscopy for evaluation of sidewalls in Type II superlattices FPAs

Fei-Hung Chu, G. A. Smolyakov, C. F. Wang, Y. Gao, C. Wang, K. J. Malloy and
A. A. Ukhanov[1]
Actoprobe LLC, 800 Bradbury SE, Suite 160, Albuquerque, NM 87106

D. V. Pete
Sandia National Laboratories, CINT, Albuquerque, NM 87185

M. Jaime-Vasquez, N. F. Baril, and J. D. Benson
US Army RDECOM CERDEC Night Vision and Electronic Sensors Directorate, RDER NVS-IF
10221 Burbeck Road, Fort Belvoir, VA 22060-5806

D. A. Tenne
Boise State University, Department of Physics, 1910 University Dr., Boise, ID 83725

ABSTRACT

Actoprobe team had developed custom Tip Enhancement Raman Spectroscopy System (TERS) with specially developed Ultra High Aspect Ratio probes for AFM and TERS measurements for small pixel infrared FPA sidewall characterization. Using this system, we report on stimulated Raman scattering observed in a standard tip-enhanced Raman spectroscopy (TERS) experiment on GaSb materials excited by 637-nm pump laser light. We explain our results by TERS-inherent mechanisms of enormous local field enhancement and by the special design and geometry of the ultra-high-aspect-ratio tips that enabled conditions for stimulated Raman scattering in the sample with greatly enhanced resonance Raman gain when aided by a microcavity to provide feedback mechanism for the Raman emission. The approach has great potential for further, orders-of-magnitude, progress in TERS enhancement by significantly increasing its nonlinear component. We report development of novel class of probes for atomic force microscopy (AFM active optical probe - AAOP) by integrating a laser source and a photodetector monolithically into the AFM probe. The AAOPs are designed to be used in a conventional AFM and would enhance its functionality to include that of the instruments (NSOM, TERS, hybrid AFM).

Keywords: TERS, Infrared Detection, AFM, Confocal Raman spectroscopy, InAs/GaSb, Focal Plane Array, Dual-band imaging, AFM Active Optical probe, AAOP, NSOM.

1. INTRODUCTION

Conventional spontaneous Raman spectroscopy is known to suffer from low efficiency and sensitivity, as it relies on the highly inefficient process of inelastic light scattering. Tip-enhanced Raman spectroscopy (TERS) combines spontaneous Raman spectroscopy with the local field enhancement capability of metallized scanning probe microscopy tip to amplify the signal by 3 to 4 orders of magnitude.[1] Stimulated Raman spectroscopy is another advanced type of Raman spectroscopy that relies on nonlinear coherent Raman scattering.[2] The most important property of stimulated Raman spectroscopy is the enormous gain in the photon emission rate over spontaneous Raman scattering enabled when the

[1] Presenting author: aukhanov@actoprobe.com

Nanoimaging and Nanospectroscopy VI, edited by Prabhat Verma, Alexander Egner, Proc. of SPIE
Vol. 10726, 107261C · © 2018 SPIE · CCC code: 0277-786X/18/$18 · doi: 10.1117/12.2504541

frequency difference between the pump field ω_p and Stokes field ω_s matches a molecular vibration. Stimulated Raman spectroscopy, however, is a very complex nonlinear technique that employs pulsed lasers with high peak powers rather than CW excitation. Stimulated Raman spectroscopy is generally performed with two synchronized (picosecond or femtosecond) pulsed lasers focused onto the same spot and requires high-frequency phase-sensitive detection to detect a small increase (stimulated Raman gain of the Stokes beam) or decrease (stimulated Raman loss of the pump beam) in light intensity at the excitation wavelengths. An enhancement factor of 9 orders of magnitude was recently reported in stimulated Raman spectroscopy aided by TERS.[3] The local field enhancement, enabled by TERS, made it possible to achieve conditions for stimulated Raman experiments with CW lasers. Still, the stimulated Raman spectroscopy experiments required two (pump and Stokes) lasers for excitation and lock-in amplified detection. Recently, the unprecedented subnanometer lateral resolution and high signal enhancement demonstrated in STM-TERS experiments under low-temperature and ultrahigh-vacuum conditions were attributed to the possible nonlinear stimulated Raman scattering process.[4, 5] As compared to AFM-TERS, STM-TERS configuration provides additional gap-mode enhancement for localized surface plasmons (LSPs) excited by incoming photons upon illumination due to the strong substrate-tip electromagnetic coupling intrinsic to STM-TERS where the sample is attached to a smooth metal substrate.[1, 6] In STM-TERS, the gap LSP modes can also be excited by electrons tunneling through the gap thus leading, after the radiative decay of the LSPs, to the STM-induced light emission, usually called STM-induced luminescence (STML).[7, 8] STML associated with very strong broadband plasmonic resonance in the Ag tip – Ag substrate nanocavity[9] and spectrally tuned to the molecular vibration by simply modifying the tip status[10, 11] was suggested as the possible source of the Stokes field ω_s to explain the observations of nonlinear STM-TERS.[4, 5]

2. EXPERIMENTAL

2.1. Confocal Raman AFM Instrument

The experimental setup was Acto-TERS, Actoprobe LLC TERS AFM instrument (Fig.1c), that combined a high-quality commercial scanning probe microscope with a special confocal Raman microscopy (CRM) system developed by Actoprobe LLC. The optical schematic of the CRM system is shown in Fig.1a. The light from a single-line high-quality commercial diode-pumped 637-nm solid-state laser was prepared in a particular polarization state using half-wave plate (HWP) to maximize surface enhancement effect on the tip apex, passed through a tunable band-pass filter (TBPF) to remove laser spontaneous emission lines, and focused onto the sample through a long-working-distance microscope objective. A 10x infinity-corrected 0.3-NA objective lens was used at 30-mm working distance for focusing the excitation laser beam onto the sample as well as for collecting the Raman signal (Fig.1b). The AFM system was operated in tapping mode with the following typical parameters: the drive amplitude was 18 mV at the cantilever resonant frequency of ~400 KHz, the tip-surface distance was ~1-2 nm and ~50 μm for the "tip-in" (tip engaged) and "tip-out" (tip retracted) conditions, respectively. The confocal microscope was configured so that the incident laser beam made and angle of 30° to the surface of the sample. The collected Raman signal was passed through a long-pass filter to remove the excitation wavelength before being coupled into an optical fiber. The optical fiber sent the Raman signal into the 4 spectrometer (Princeton Instruments Acton SpectraPro SP-2500) with 2400 g/mm grating.

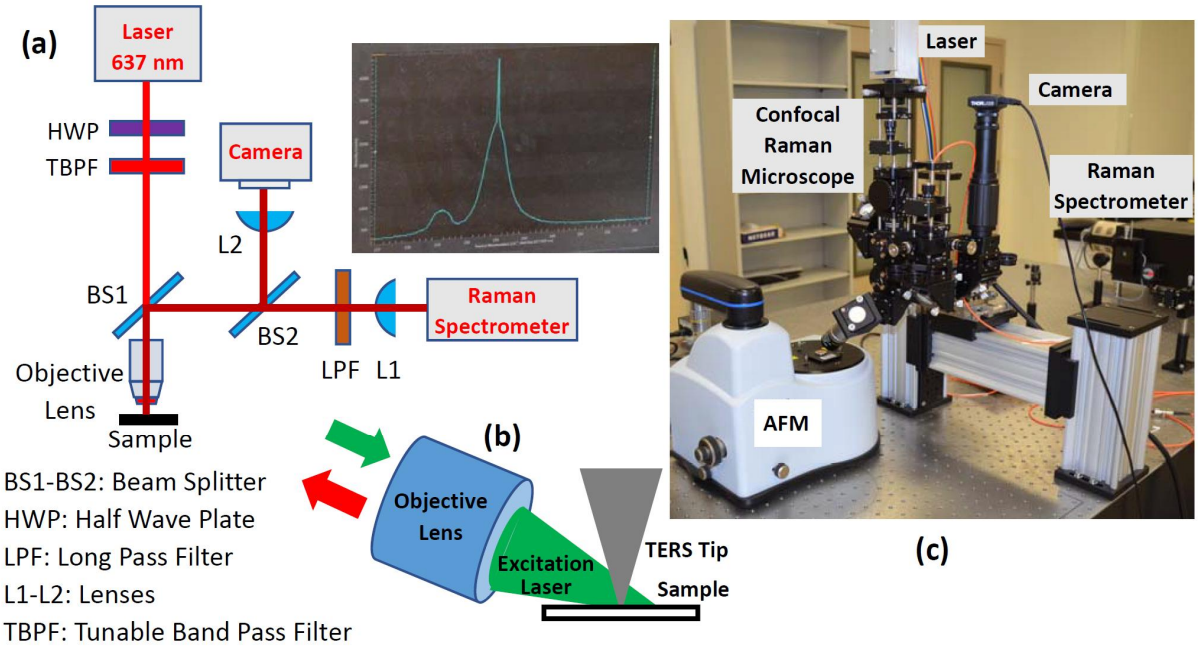
(a)
Laser
637 nm
HWP
TBPF
Camera
L2
BS1
BS2
LPF
L1
Raman
Spectrometer
Objective
Lens
Sample
BS1-BS2: Beam Splitter
HWP: Half Wave Plate
LPF: Long Pass Filter
L1-L2: Lenses
TBPF: Tunable Band Pass Filter
(b)
Objective
Lens
Excitation
Laser
TERS Tip
Sample
Laser
Camera
Confocal
Raman
Microscope
Raman
Spectrometer
AFM
(c)

AFM sidewall characterization of MWIR and LWIR T2SL FPAs is difficult with conventional AFM probes. Their low aspect ratio does not allow them to reach into the deep trenches of the FPAs. The Actoprobe team developed its own High Aspect Ratio AFM probes to accomplish this challenging task.

Standard (low aspect ratio) Si probes were mounted in the sample holder of FIB vacuum chamber equipped with a Gemini Column for e-beam imaging and a Ga gun for ion-milling. Ion currents of 50-500 pA were applied for milling, and the current and milling time were changed according to the dose. A lower current was used to sharpen the probe tip. We also fabricated Pt coated probes for conductivity measurements. The Pt was supplied as Pt organometallic gas through a nozzle. The nozzle allows a controlled deposition of Pt on the probe tip either by e-beam or by ion-beam. The Pt coating also reinforces the contact between the tip and the cantilever, which might be beneficial for very thin cantilevers. Specific characteristics of the high aspect ratio probes such as length, tip aperture and tip radius depend to some extent on the low aspect ratio AFM probes from which they were made. Here we present high aspect ratio probes fabricated from different commercially available probes: PPP-NCRL Nanosensors^{TM}, VeecoUltralever, and AppNano ACCESS-FM-A. SEM images of high-aspect-ratio probes fabricated by Actoprobe are shown in Figs. 2a, 2b. Fig. 2 presents our special design for easy access to the probe tip. This probe geometry is especially advantageous for upright collection of the signal. Collecting the signal vertically from the probe tip is by far more convenient and reliable than doing that at an angle (since oblique collection is bound to produce weaker signals and optical alignment is much more difficult). Another special design of holey probes for easy light coupling to the probe tip is shown in Figs. 3. We modified previously fabricated AFM probes into holey probes such that light from an external laser source could be coupled into the back of the tip. This was achieved by removing the metal coating on the cantilever in a circular area exactly above the probe tip, using FIB. Figs. 3a shows a Veeco Ultralever probe (ULCT-AUMT-A) modified as described above. Fig. 3b presents a modified AppNano ACCESS-FM-A AFM probe – a holey probe with easy access to the probe tip. Fig. 4 shows yet another special design of NSOM AFM probe with two apertures (openings), one on the top and one on the bottom, to couple visible laser light into the probe.

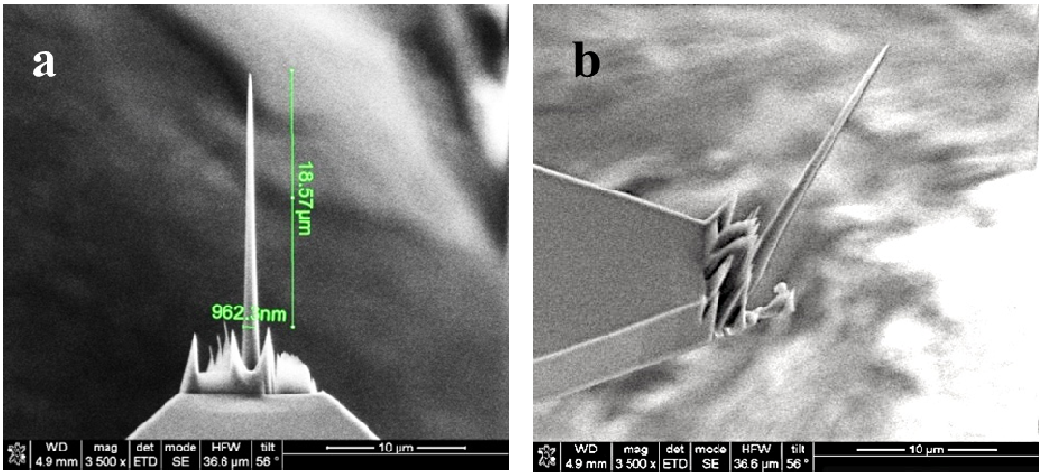

Figure 2. Two SEM images of high-aspect-ratio probe tips with easy access to the probe tip fabricated by FIB of convencional ACCESS AFM probes: sideview (a) and titled view(b).

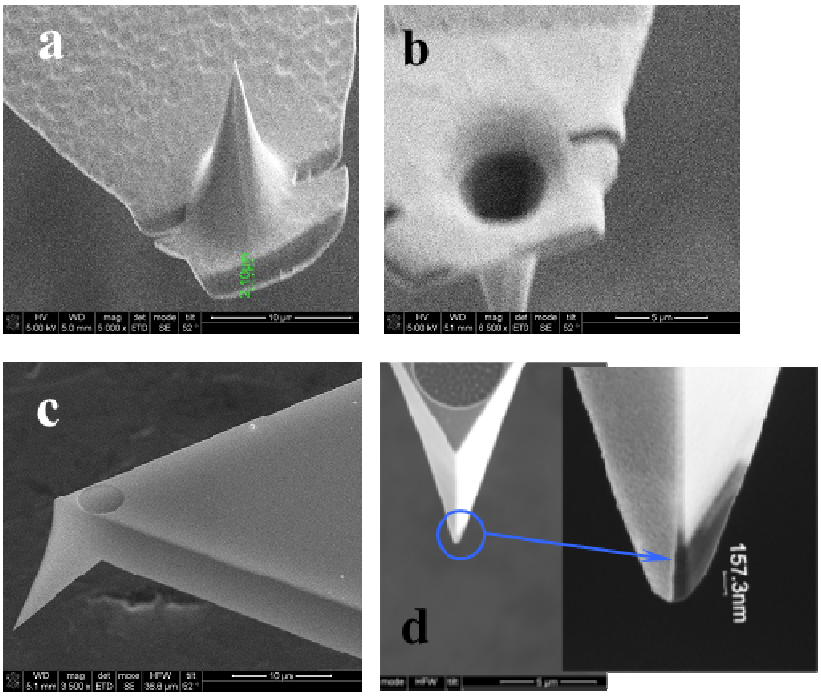

Fig. 3. (a).Veeco Ultralever AFM probe with the edge of the cantilever cut off. Image (b) is Veeco Ultralever AFM probe with the metal removed in a circular area above the tip. (c) AppNano ACCESS-FM-A AFM holey AFM probe. (d)Side view of the tip apex with an opening in Au coating at the end of the tip.

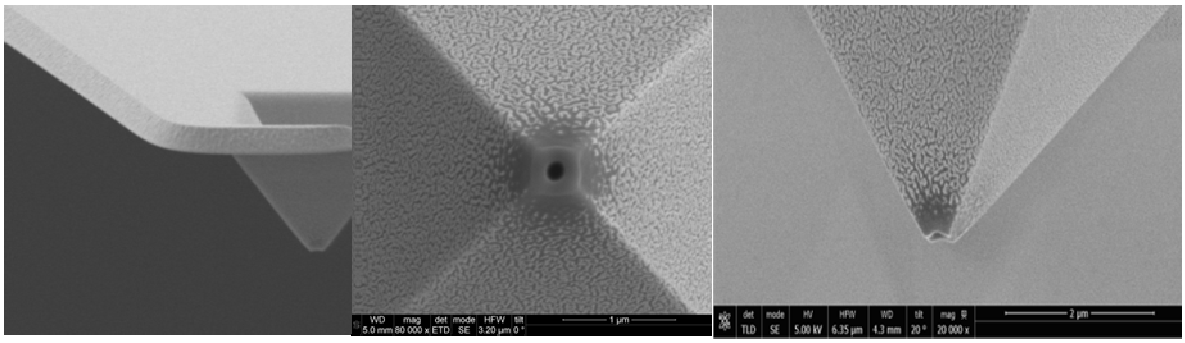

Fig. 4. NSOM AFM probe with two apertures (openings), one on the top and one on the bottom, to couple visible laser light into the probe

2.3. AFM Active Optical Probe

Optical characterization at the nanoscale currently requires instruments such as NSOM (near-field scanning optical microscope), TERS (tip-enhanced Raman spectroscopy), or hybrid AFM (that includes a specialized far-field optical microscope). AAOP is fabricated on a III-V substrate and combines diode laser and detector inside the AFM probe. Therefore, no external laser excitation is required for TERS and NSOM., which help reduce the alignment effort. The AAOP concept is based on combining a diode laser and an AFM probe monolithically.

The AFM Active Optical Probe (AAOP)[14] is shown in Figure 5. In this Figure we present a cross-sectional view of the probe, a side view and a bottom view. The AAOP consists of a cantilever 10 with the AFM probe tip 11 mounted on a conventional Si chip 12 (3.4 mm × 1.6 mm × 0.3 mm). The AAOP is designed as an intra-cavity probe, i.e. the AFM probe is part of the laser cavity as shown in an equivalent optical schematic of the device in Figure 6. This increases laser

light coupling into the optical near field at the apex of the AFM probe by a factor of 10,000.[15] The AAOP is a very efficient optical near-field nano-emitter.

The most widely used probes for atomic force microscopy are fabricated using silicon technology. In contrast, the AAOPs are fabricated from GaAs, a semiconductor material suitable as the basis for optical device fabrication. The laser and detector functionality is enabled by an epitaxially grown structure. Ridge-waveguide laser diode and efficient photodetectors are fabricated by patterning the active region 13 (epi-layer), while the AFM tip 11 is fabricated from the GaAs substrate 14 at the end of a cantilever 10 formed from the epi-layers of the laser structure. The cantilever with the AFM probe is fabricated from an epitaxial laser structure MBE-grown on a GaAs substrate. The laser 15 is designed as an electrically pumped edge emitting laser (ridge waveguide), and the epitaxial structure is a typical quantum well edge emitter structure with 10-nm wide Ga0.85In0.15As quantum wells imbedded in a GaAs waveguide and surrounded by doped Al0.7Ga0.3As cladding layers, one of them is n-doped and the other p-doped. The structure also includes an Al0.95Ga0.05As etch stop layer to facilitate substrate removal in order to fabricate a cantilever that consists only of the ~ 5-μm thick epitaxial laser structure. The choice of GaAs is motivated by the large base of established fabrication technology, which allows for time- and cost-effective fabrication of the probes. Practice of the present invention can be easily extended to alternative III-V semiconductors such as InP, GaP, GaSb, and GaN to expand the available wavelength coverage from UV to visible and mid-infrared.

The first laser mirror, mirror #1, is a standard first-order DBR grating 16 (period λ/2neff, where λ is the laser wavelength and neff is the effective refractive index of the GaAs waveguide) that ensures single longitudinal mode for the laser operation. Light generated by the laser is coupled into the surface mode of the GaAs probe (conic shape micro-prism) and transferred to the tip apex as follows: at the end of the cantilever and inside the laser cavity, mirror #2, a second-order DBR grating 17 (period λ/neff), couples the light (an intracavity laser mode) vertically into the AFM tip. It serves as a folding mirror.

The tip 11 itself is a Total Internal Reflection Prism (TIRP) and plays the role of an output mirror, mirror #3, in the laser cavity. The GaAs micro-prism guides the laser light into the tip apex and generates a strong surface optical mode at the GaAs/air interface. It creates a high magnitude optical field highly localized at the apex of the AFM tip, sufficiently strong to enable effective excitation for nano-scale Raman Spectroscopy – Tip Enhanced Raman Spectroscopy (TERS). Finite Difference Time Domain (FDTD) simulations predict that for a bare GaAs micro-prism the near-field light (λ = 980 nm) can be focused to a spot size of 160 nm in diameter and with about 30 mW power. By coating the micro-prism with a thin layer of gold 18 (50 nm), the spot size decreases to dimensions less than 50 nm but the power reduces by a factor of about 1000. Depending on application, the probe can be apertureless or have a nanometer-size aperture at the apex. In the case of the apertureless probe, a surface plasmon mode is excited in the Au coating, providing a very strong optical field at the apex of the AFM tip. In the case of the probe with a nanometer-size aperture, the tip operates as an optical waveguide below cut-off frequency and optical radiation is transmitted through the aperture.

The fabricatied GaAs probe tip **11** had a conical geometry with 40° angle and a base of 10 − 12 μm (FIG.6). This geometry makes this probe an optical antenna that focuses laser radiation into a diffraction limited spot of 280 nm diameter for a laser wavelength of 1 μm as a result of total internal reflection in the GaAs conical waveguide with no cutoff losses. Additional metallization of the conical waveguide with gold of 80-nm thickness will provide additional focusing of the light to about 40 − 20 nm in diameter[16] because of the surface plasmon effect. Systematic design of probe tip using FDTD simulations revealed that introduction of well-controlled asymmetry in the probe tip configuration combined with asymmetry in illumination of probe tip and light polarization should enable substantially improved resolution of the near-field probe up to ~ $\lambda/20$ - $\lambda/30$. An example of such asymmetric probe tip is a 4-sided high-index (n ~ 3.5) pyramid (GaAs or Si) conformally covered with 80 nm-thick Au, except for the last 20 nm of one side of the pyramid close to the tip that is left uncoated. FIG.5 shows a cross section of such a probe **11** asymmetrically coated with a layer of gold **18**.

For conventional TERS, the far-field optical power is on the order of 20-100 mW. Since with the AAOP, the light can be coupled to the near field more efficiently, substantially less optical power is necessary to obtain the same electric field strength at the tip apex. We estimate that an optical power in the range of 0.5 - 10 mW is sufficient, and can easily be provided by semiconductor lasers.

The main difference of the AAOP from other AFM probes is that the AAOP is designed to do optical nano-scale spectroscopy together with AFM imaging. Front- and back- sides of the chip are metallized in the appropriate places to make electrical contact to laser/detector structure and to provide high reflectivity for optical displacement monitoring used to read out tip deflection for AFM imaging. Electrical contact can be realized by means of a hole **19** etched through the Si chip **12** and filled with metal.

This optical AFM probe utilizes the diode laser operating in pulsed mode under direct modulation of the injection current with low duty-cycle (~ 1 − 5%) to avoid heating of the AFM tip and imaging artifacts related to heating.
The AFM cantilever dimensions (see FIG. 5) are chosen to provide performance similar to that of conventional Si AFM probes and accommodate the laser diode cavity and photodector structures. Both the laser and photodetector epitaxial structures are identical but differ in terms of the biasing: the laser diode junction is biased in forward direction (electrons and holes recombine and create light); the reverse bias applied to the photodetector creates a depletion region where incident light will create electron/hole pairs, producing a photocurrent proportional to light intensity.
The AFM tip **11** is located directly underneath the second-order DBR grating **17**. The light radiates from the apex of the tip that forms a point source. The tip is located between two photodetectors **20** that consist of stripes similar to the laser ridge waveguide but reverse-biased (FIG.9). The large detection area of about 50 × 100 μm^2 each provides high light collection efficiency. This point source, which is a source of light scattered from the sample under investigation, are less than 10 μm away from the detector. This close proximity of the source and the detectors also provides high collection efficiency for scattered near-field radiation. Second-order DBR gratings **21** fabricated on top of the photodetector structures couple the light scattered from the sample into the ridge waveguide photodetectors. By applying a voltage the effective refractive index can be slightly altered , thereby tuning the DBR grating for a specific Raman shift. By sweeping the voltage, this structure can work as a Raman spectrometer without moving parts.

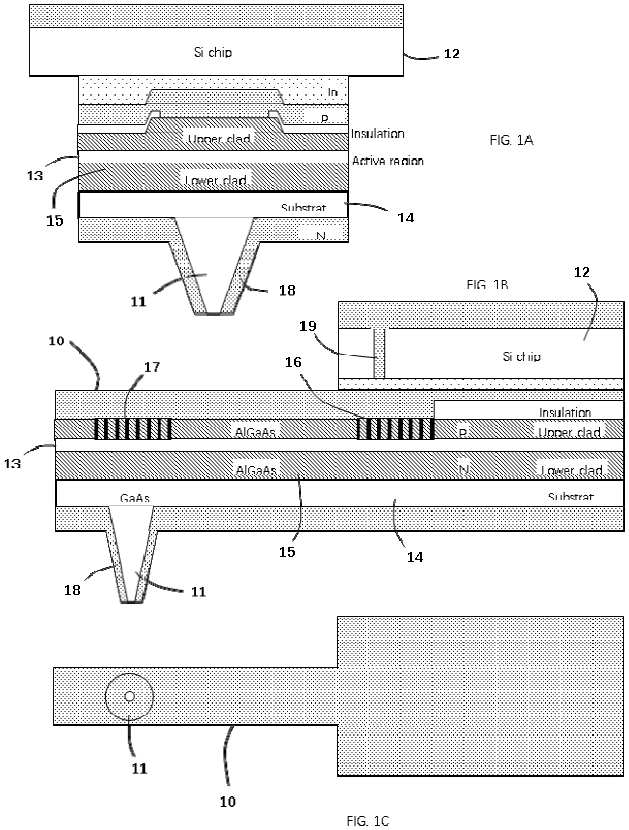

Fig. 5. FIGS. 5A, 5B, and 5C are schematic illustrations of Embodiment 1 of an AFM active optical probe according to the invention, showing its configuration: (A) cross-sectional view, (B) side view, and (C) bottom view.

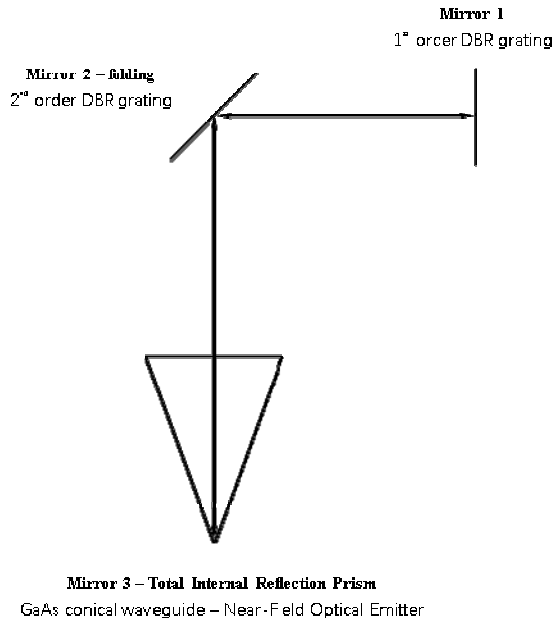

Fig. 6. A schematic illustration of the AAOP optical scheme

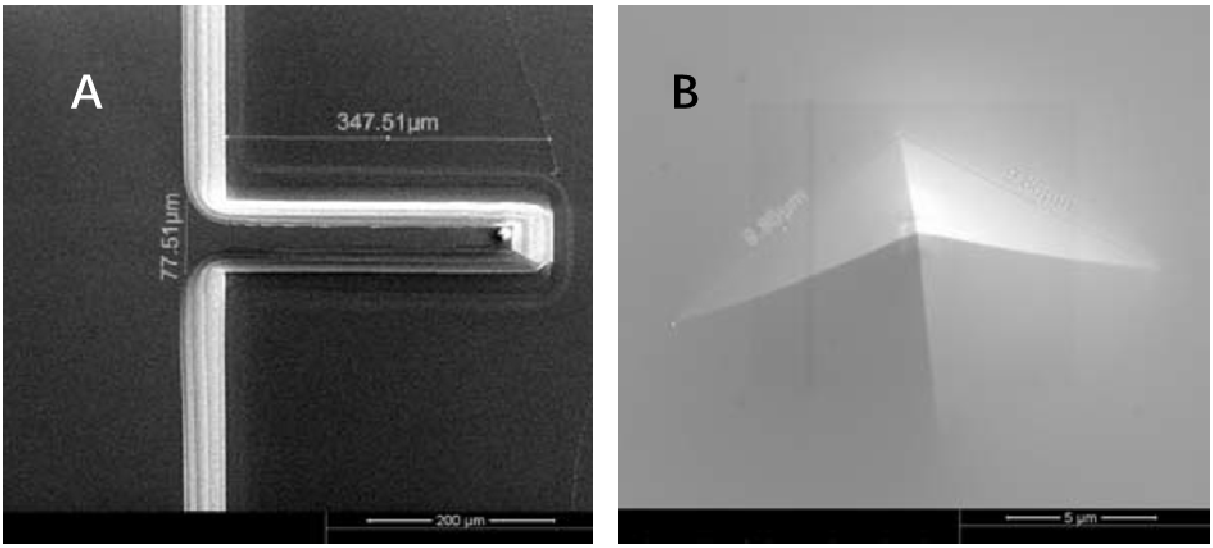

FIG. 7.7A is top view of a GaAs AFM cantilever with the tip fabricated using wet chemical etching. The cantilever has not been separated from the substrate. And 7B is a close-up view of the tip tilted 25°. The base of the tip is about 10 µm ×10 µm. The tip radius achieved here is on the order of 50 nm

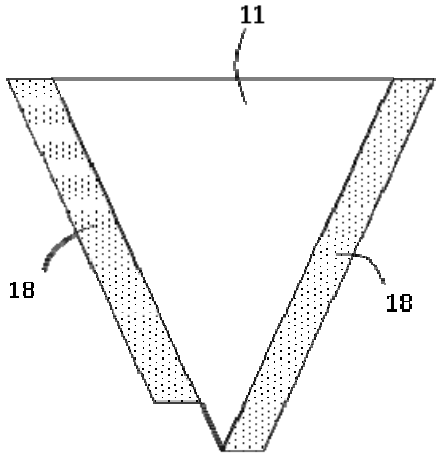

FIG. 8 is a chematic illustration of an asymmetric probe tip concept.

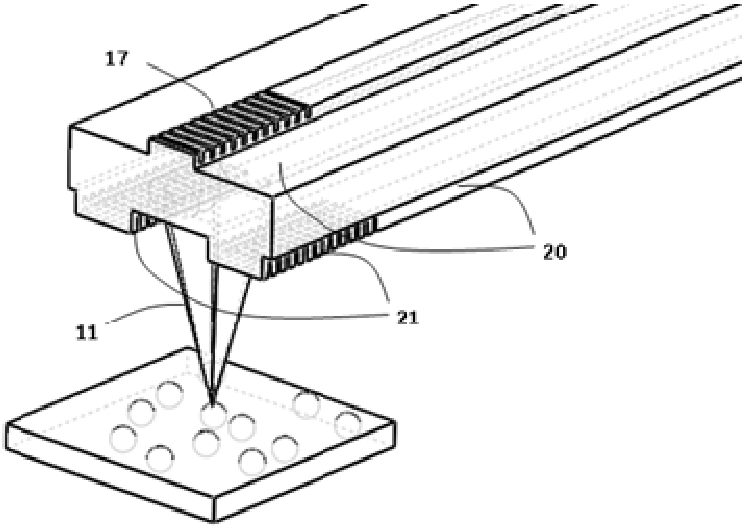

FIG. 9 is a 3-D illustration of the AAOP concept.

To verify the device cut-off wavelength, single element detectors were fabricated. Device fabrication was initiated with standard optical photolithograpy to define 410 µm x 410 µm square mesa devices with apertures ranging from 25 to 300 µm.The mesas were etched by ICP with a BCl_3 - based chemistry to an etch depth of ~ 9 µm, which corresponds to the middle of the bottom contact layer. Next, ohmic contacts were evaporated on the bottom and top contact layers using Ti (500 Å) / Pt (500 Å) /Au (3000 Å) in both cases.

Finally, the devices were passivated by SU-8 2002 photoresist after a short (40 seconds) dip in a phosphoric acid based solution (H_3PO_4:H_2O_2:H_2O = 1:2:20) intended to remove the native oxide film formed on the etched mesa sidewalls.

After fabrication, the devices were diced and mounted on 68 pin leadless chip carriers (LCC) for further characterization. Spectral response measurements were performed at 68 K with a Fourier transform IR spectrometer (FTIR) equipped with a glow-bar black body source. The detector spectral response curves, shown in Fig.10, were similar for both negative and positive bias polarities, as expected from the device design. The measured 50% cut-off wavelengths were ~ 10.7 μm and ~ 10.4 μm for the negative and positive applied biases, respectively (at 68 K).

To provide feedback on the morphology and chemical composition of etched and passivated sidewalls of the LWIR T2SL detectors with smaller features, 24 μm x 24 μm mesas of 320 x 256 FPA were delineated from the same T2SL material with BCl_3-based ICP.

2.4. FPA material growth and fabrication

The detector material[34], on which the AFM/TERS measurements were performed, was grown on an n-type (Te-doped) GaSb (001) epi-ready substrate using elemental source molecular beam epitaxy (MBE) in a Veeco GEN 10 system equipped with valved cracker sources for group V (Sb_2 and As_2) and Ga/In SUMO® cells. The device structure is composed of two 4-μm thick T2SL absorbers with the same cut-off wavelength (~ 9 μm at 68K) separated by a 100-nm barrier layer. The LWIR absorbers as well as the barrier layer were p-type doped with carrier concentrations of 1×10^{16} cm^{-3}. The p-type (2×10^{18} cm^{-3}) bottom contact layer with the same T2SL composition and thickness as the LWIR absorbers was grown on a 200-nm thick p-type (2×10^{18} cm^{-3}) GaSb buffer layer. The top contact layer (150-nm thick), with the same T2SL composition and doping level as the bottom contact layer, capped the structure.

3. RESULTS AND DISCUSSION

3.1. Polarization dependence in Raman Spectroscopy of FPA Sidewalls

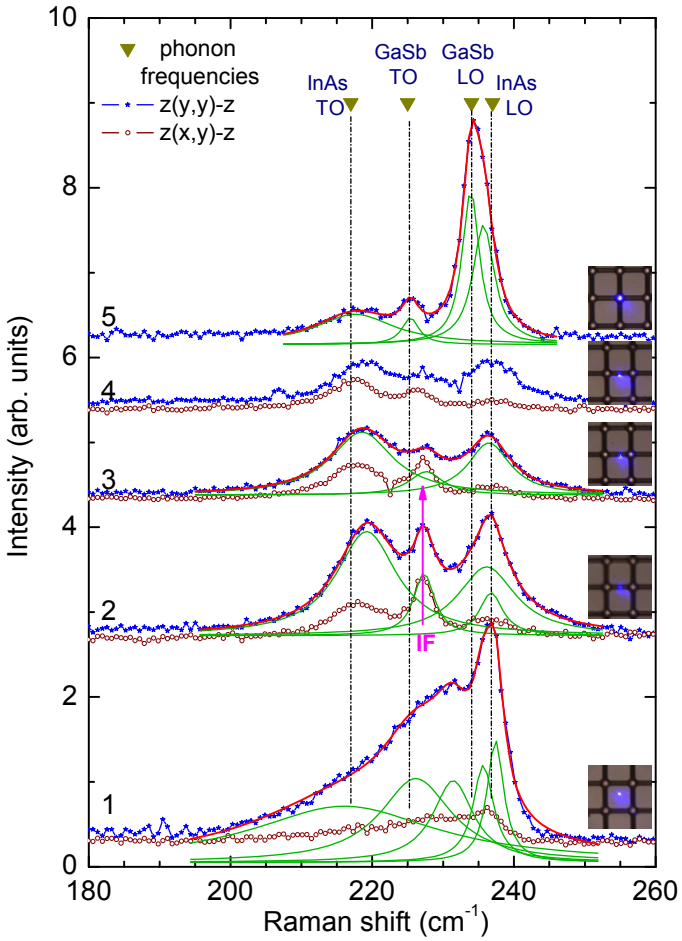

Fig. 10. Micro-Raman spectra of T2SL-FPA structure measured at different points in **backscattering normal to the SL layers** in parallel $z(yy)\bar{z}$ and perpendicular $z(xy)\bar{z}$ polarization geometries. Lorentzian fitting was performed to distinguish different phonon features in the spectra (red lines - fitting results; green lines - contributions from individual phonon modes). The inset images show the location of the laser spots corresponding to the measured spectra. Triangles show the TO and LO phonon frequencies in bulk GaSb and InAs. Dashed lines are guides to the eye.

Micro-Raman spectra of the 24 μm x 24 μm mesa of T2SL FPA with 6.7-μm etch depth are shown in Fig.10. The spectra were measured at different points of the sample: the center of the mesa (1), the center of the etched trench (2), two points on the sidewall (3,4), and the crossing of the trenches (5). Spectrum 1 corresponds to the unetched SL, the strongest features are associated with the LO phonons of InAs and GaSb. This is in agreement with the Raman selection rules: in crystals of zinc blende structure only LO phonons are allowed in backscattering from (001) surface. The LO phonon frequencies of GaSb and InAs are close (236 and 239cm^{-1}, respectively, and are not resolved, appearing as a single peak at ~237 cm^{-1} in spectra 1. It should be noted that the SL thickness is much larger than the penetration depth of the laser light, therefore the substrate signal is suppressed in the spectra taken from the unetched region. In contrast, spectrum 5 (from the deepest etched area) is dominated by the LO phonons of GaSb, associated with the GaSb substrate, so the strongest peak is shifted to lower frequency. InAs phonons are still present at lower intensity, which is probably due to the contribution of nearby sidewall regions.The spectra from the sidewall regions (2-4) show equally strong features of LO and TO phonons. This is due to the deviation from backscattering geometry along the (001) direction. Sidewalls form an angle of about 70° to the SL layers plane. Due to large index of refraction ($n \approx 3.9$ for both InAs and GaSb), light enters the structure at an angle of ~30° from the layers plane. Thus, the wave vectors of phonons participating in Raman scattering have large component parallel to the layers, and light polarization vectors can have components both along and perpendicular to the surface, so the TO phonons become Raman active. Another feature also appears in the spectra taken from the sidewall regions at ~227 cm^{-1}. This may look like GaSb TO phonon, but the latter

appears in spectra at lower frequency (225 cm, as seen in spectrum 5). We believe this feature should rather be attributed to interface phonons (labeled IF in Fig. 11), although a contribution of GaSb TO phonons cannot be excluded. These vibrations, well known in superlattices are localized near and propagating parallel to the interfaces. Both TO and IF modes require a wave vector component parallel to the SL layers, thus their intensity is increased in the sidewall regions. Peaks associated with LO phonons in the sidewall spectra are significantly broader compared to the unetched pixel top. This is due to structural disorder (poorer crystalline quality) on the sidewalls resulting from etching damage.

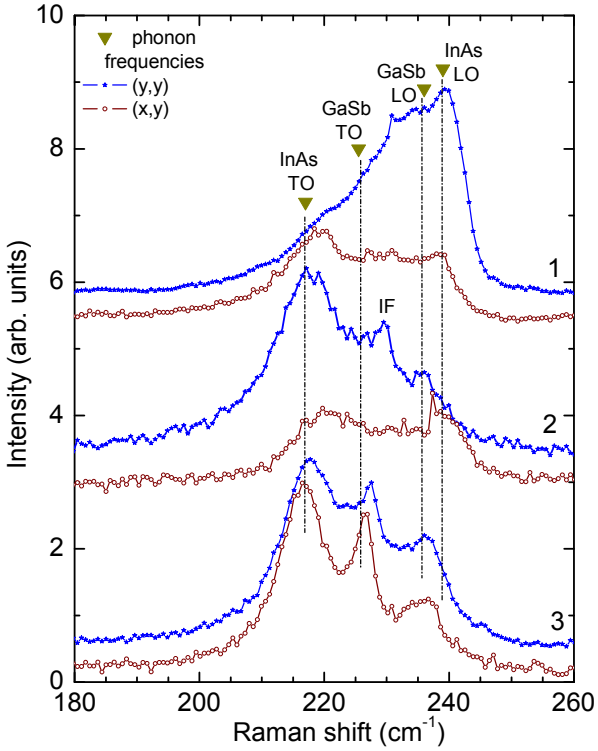

Fig. 11. Micro-Raman spectra of T2SL-FPA structure measured at different points **in oblique geometry**: excitation at ~60° with respect to the vertical axis z, (normal to the SL layers) with collection along z axis in parallel $z(yy)\bar{z}$ and perpendicular $z(xy)\bar{z}$ polarization geometries. Numbers indicate the location of laser spots, corresponding (approximately) to those shown in the inset images of Fig. 11. Triangles show the TO and LO phonon frequencies in bulk GaSb and InAs. Dashed lines are guides to the eye.

Fig. 11 shows Raman spectra from three different points of the sample measured at oblique incidence. The locations of laser spots correspond approximately to the points 1 (center of the mesa), the center of the etched trench (2), and the middle of the sidewall (3) of Fig.11. The spectra are generally similar to those shown in Fig. 11, but the peaks of TO phonons are enhanced with respect to the LO phonons, especially in the sidewall regions, where light enters the sample nearly parallel to the layer, thus activating TO and interface phonons. The spectra show differences in different polarization geometries, however, the interpretation is more complicated, as polarizations are mixed due to oblique incidence.

The analysis of the Raman spectra shown in Fig. 11 and 12 illustrates that TO phonon peaks can be utilized for characterization of the pixel sidewall quality. Raman peaks corresponding to both InAs and GaSb phonons carry information about material quality on the pixel sidewalls, as the latter affects boundary conditions. This information is contained in both peak intensity and width. One can see (Fig. 11) that the peak width is increased at the sidewalls compared to the pixel top, likely due to defects introduced by the plasma etching process. When laser is focused on the sidewall, due to large index of refraction, light enters the structure with large component of wave vector parallel to the layers. Light polarization vectors have components both along and perpendicular to the surface, making both TO and LO phonons Raman active. LO phonons involve vibrations mostly normal to the surface, so are probably less affected by the surface structure, while TO phonons polarized parallel to the surface may be more sensitive to the surface defects.

However, it is important to note, that most of the signal comes from the areas away from the surface (excitation depth ~8.5 nm), therefore there is a need to increase surface sensitivity (e.g. by utilizing UV light with shorter penetration depth).

3.2. AFM Tip-enhanced stimulated Raman scattering using Actoprobe High Aspect Ratio Probes

Actoprobe's TERS system can also be used for NSOM experiment as shown in Fig.12 with the red laser (637nm). The AFM image shows the conventional AFM scan of the FPA sample and the corresponding NSOM image is taken at the same time as AFM scan. NSOM data shown below in Figure 12, obtained with our UHAR probes also demonstrate that we achieved 20nm lateral resolution in our experimental TERS setup.

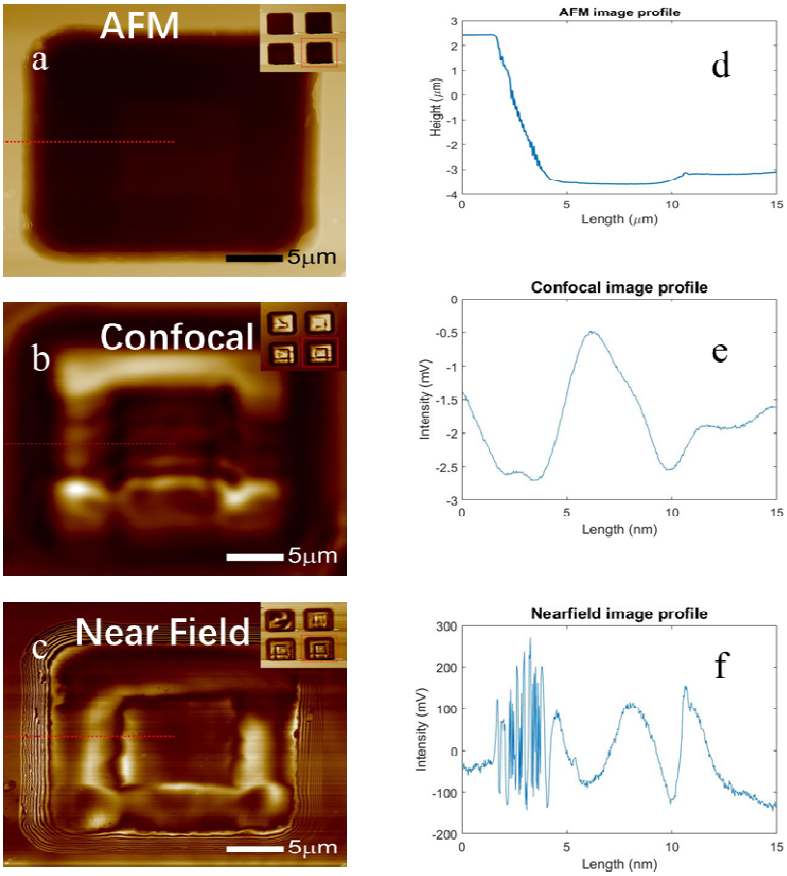

Fig. 12. AFM (a), confocal (b) and near‐field (c) images of a focal plane array test sample. Image size is 35µm square. Insets show larger area of the test sample. Three different profiles (d-f) shown in the right are measured on the corresponding images from the center to the edge of the images.

In the figure below (Figure 13), the intensities of TO and LO spectral lines vary along the sidewall of the focal plane array due to material composition variations and changes in optical polarization orientation relative to the surface. The Raman signal is significantly enhanced for the TO phonon. The TO and LO spectra vary along the sidewall due to material composition change and optical polarization relative to the surface, as shown in Fig. 13a. The spectra change along the sidewall also confirms twenty nanometer spatial resolution of Actoprobe's TERS system, as shown in Figure 13b.Such high spatial resolution –equal to the TERS tip size is only possible when near‐field contribution dominates in the Raman signal.

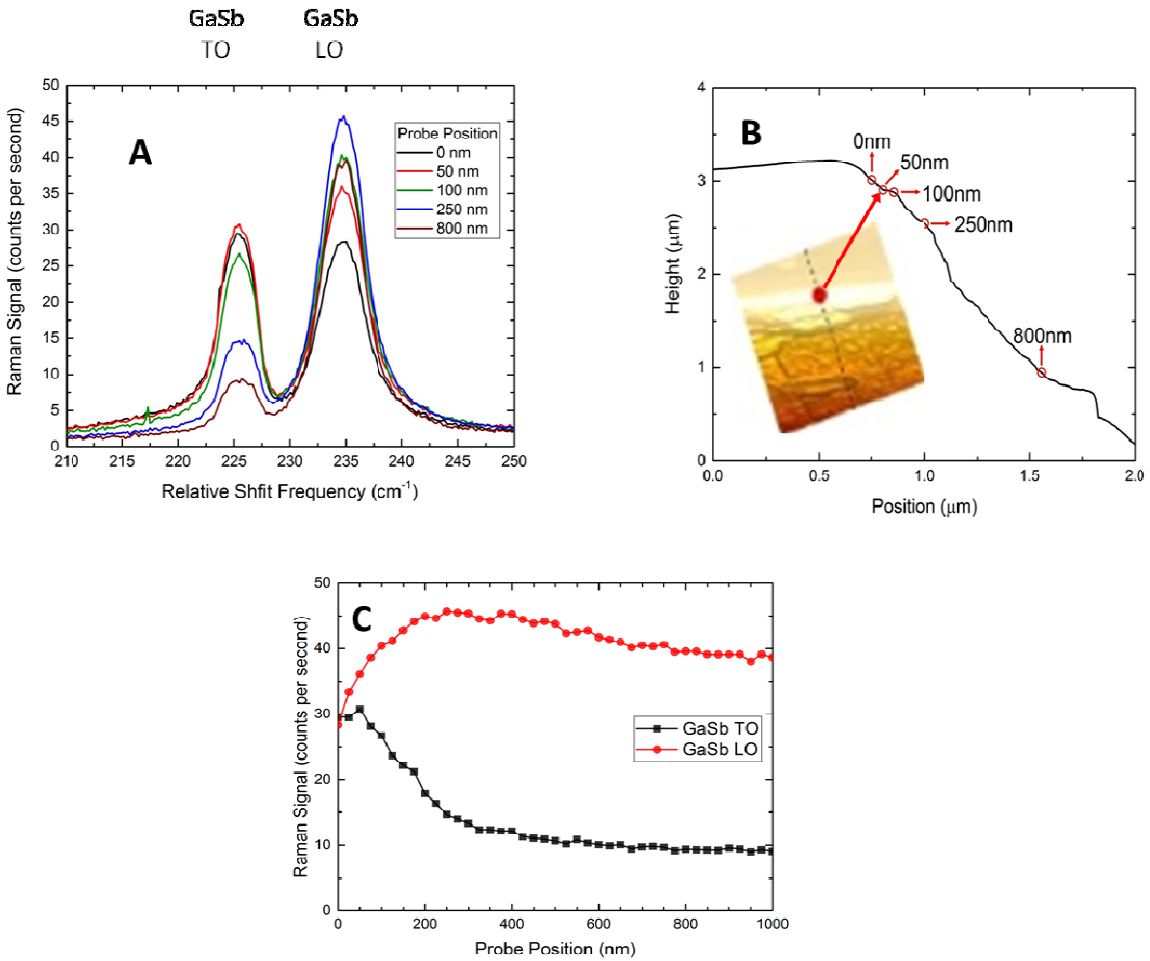

Fig. 13. A is the Position‐dependent Raman spectra. B is Positions along FPA side wall where Raman spectra were taken and C is Intensities of GaSb TO and LO spectral lines as extracted from position‐dependent Raman spectra.

The possibility of increased contribution from far-field when tip is engaged should be considered when calculating the enhancement factor.17 As it was mentioned in the paper, this increase in far field depends on many factors including reflectivity of the tip shaft, tip geometry, roughness of sample surface, illumination geometry, and tip-sample configuration. In our experiments, TERS measurements were performed on an epitaxially grown sample with very flat and smooth surface of GaSb top layer, providing very little Rayleigh scattering. At the same time, in the oblique TERS geometry, the smooth surface results in specular reflection with practically all the unabsorbed excitation light being reflected away from the tip shaft and tip base. We find any significantly increased far-field contribution in the tip-engaged configuration to be unlikely under these specific experimental conditions. The actual field enhancement at the tip apex was confirmed by TERS measurements with our UHAR probes that demonstrated spatial resolution better than 20 nm.

In Fig. 14 we show results obtained from TERS experiments performed at the bottom GaSb surface of a deep focal-plane-array (FPA) trench.15 UHAR tips were used coated Laser with nominal 25 nm, 50 nm, 75 nm, 100 nm, and 125 nm of gold. The estimated values for TERS contrast and enhancement factor in each case are shown in Table 1.

Table 1. TERS contrast and enhancement factor estimated for tips with different thickness of gold coating

Gold coating thickness	Contrast	Enhancement factor
Probe 1, 25 nm	12.6 %	126,000
Probe 2, 50 nm	22.3 %	223,000
Probe 3, 75 nm	81.9 %	819,000
Probe 4, 75 nm	65.6 %	656,000
Probe 5, 100 nm	12.4 %	124,000
Probe 6, 125 nm	11.6 %	116,000

TERS enhancement factor was calculated as:[17]

$$F_{TERS} = \left(\frac{S_{in}}{S_{out}} - 1\right)\left(\frac{V_{FF}}{V_{NF}}\right)\cos\alpha\,, \quad (1)$$

($S_{in}/S_{out} - 1$) represents the contrast. The area of the focus A_{FF}, the area of the near-field contributing to TERS A_{NF}, effective depth of focus (from which Raman scattering is collected) h_{FF}, and effective depth of near-field h_{NF} were estimated to calculate $V_{FF} = A_{FF}\, h_{FF}$ and $V_{NF} = A_{NF}\, h_{NF}$. The area of the focus A_{FF} was estimated as $A_{FF} \approx 2.5 \times 10^6$ nm^2 directly from images of the laser focus obtained with calibrated CCD camera. The effective area of the near-field can be estimated as $A_{NF} = \pi(R_{tip}/2)^2$. The radius of the tip R_{tip} was measured from SEM images of 10 UHAR probes and the average value $R_{tip} \approx 9$ nm was used in calculations of the enhancement factor. This value is consistent with the spatial resolution better than 20 nm obtained in Raman imaging experiments, which is known to be determined by the tip diameter. The depth of the focus and the optical penetration depth have to be considered and the smaller value of these two parameters to be used to estimate h_{FF}. We found the optical penetration depth to be much smaller than the depth of focus for GaSb strongly absorbing at 637 nm. The extinction coefficient k = 1.09 and related absorption coefficient $\alpha = 2.1503 \times 10^5$ cm^{-1} for GaSb at 637 nm gave us the optical penetration depth of ~ 100 nm calculated at 1/10 intensity level, so we estimated $h_{FF} \approx 100$ nm. The effective depth of near-field h_{NF} depends on the extent of the enhanced field around the tip in the z direction. We estimated this parameter as $h_{NF} \approx 2$ nm. The maximum TERS contrast and enhancement were observed for the tips coated with 75 nm of gold where the optimal conditions for excitation of localized surface plasmons with 637 nm laser light were achieved.

The possibility of increased contribution from far-field when tip is engaged should be considered when calculating the enhancement factor.[18] The increase in far field depends on many factors including reflectivity of the tip shaft, tip geometry, roughness of sample surface, illumination geometry, and tip-sample configuration. In our experiments, TERS measurements were performed on an epitaxially grown sample with very flat and smooth surface of GaSb layer, providing very little Rayleigh scattering. At the same time, in the oblique TERS geometry, the smooth surface results in specular reflection with practically all the unabsorbed excitation light being reflected away from the tip shaft and tip base. We find any significantly increased far-field contribution in the tip-engaged configuration to be unlikely under these specific experimental conditions. The actual field enhancement at the tip apex was confirmed by TERS measurements with our UHAR probes that demonstrated spatial resolution better than 20 nm.

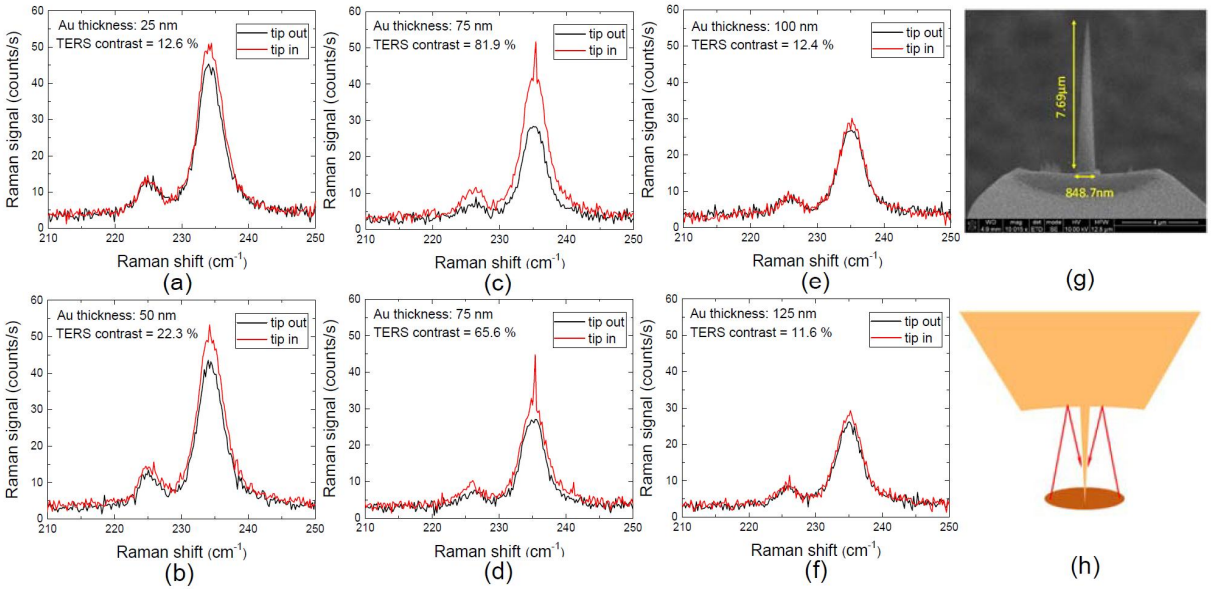
Au thickness: 25 nm
TERS contrast = 12.6 %
tip out
tip in
Raman signal (counts/s)
Raman shift (cm-1)
(a)
Au thickness: 75 nm
TERS contrast = 81.9 %
(c)
Au thickness: 100 nm
TERS contrast = 12.4 %
(e)
7.69μm
848.7nm
(g)
Au thickness: 50 nm
TERS contrast = 22.3 %
(b)
Au thickness: 75 nm
TERS contrast = 65.6 %
(d)
Au thickness: 125 nm
TERS contrast = 11.6 %
(f)
(h)

reflected back to the tip where it gets locally enhanced by the plasmonic tip and, if not reflected from the sample surface, is injected into the sample area under the tip apex, stimulating the generation of Stokes photons in the medium with very large Raman gain (Fig. 14h).

The spectral narrowing of the Raman line observed in our experiments is also characteristic of Raman generators and Raman lasers. Spontaneous Raman scattering reproduces the linewidth of the Raman transition, whereas in SRS, the Raman gain is highest at the line center, and thus spectral narrowing occurs as the gain is increased.[20] The larger the Raman gain, the shorter the propagation distance for the Stokes light through the amplifying medium for spectral narrowing to occur. With the very short, nanometer-scale, propagation distance through the active medium in our case, we consider the observed spectral narrowing of the Raman line as the sign of very large Raman gain existing in the very small volume of the sample probed by the tip-enhanced local near field.

SRS depends on the pump intensity and Raman gain coefficient, proportional to Raman scattering cross section and inversely proportional to the linewidth of the corresponding Raman line. First, we estimate the pump intensity conditions. For 25 mW incident power and AFF ≈ 2.5 μm^2, the average intensity in the focal area is I_{FF} ≈ 1x10^6 W/cm^2. Assuming the enhancement for the excitation light and for the Raman scattered light to be approximately the same, the TERS enhancement factor can be approximated by FTERS ≈ g^4, where g = E_{tip}/E_0, E_{tip} is the electromagnetic (EM) field strength at the tip, and E0 is the EM field strength at the sample with the tip retracted. For the maximum observed FTERS of ~656,000 to ~819,000 for tips coated with 75 nm of gold, the local intensity underneath the tip will rise by a factor of g^2, that is by a factor of ~800 to ~900, with the local near-field intensity INF = IFF g^2 reaching the level from ~800 to ~900 MW/cm^2.

In polar semiconductors, exciton-mediated resonant Raman scattering can lead to several orders of magnitude enhancement in Raman cross section as compared to that observed in spontaneous Raman scattering in highly transparent materials.[21-23] Additional several-fold enhancement of Raman cross section was reported in polar semiconductors doped with various kinds of impurities24. In our experiments, laser excitation of GaSb, polar semiconductor, at 637 nm provided conditions for resonant Raman scattering, with the photon energy of 1.946 eV exceeding the GaSb bandgap of 0.726 eV by 1.22 eV and the corresponding very large absorption coefficient α ≈ 2.15 x 10^{5}cm^{-1}. We expect, therefore, Raman gain to be orders of magnitude larger in our experiments on heavily doped GaSb excited above the bandgap as compared to similar experiments done on highly transparent samples. SRS observed in highly transparent materials relies on very low spontaneous Raman gain achievable in such material, as determined by very low Raman cross sections. A combination of high pump intensity and/or very long effective path length for the Stokes shifted photons in the active Raman material is required to observe SRS in such situations. In microcavities, SRS enhancement occurs due to pump intensity build up in the cavity. Still, microcavities of very high quality (Q factor) are required to ensure a very long effective path length $\mathbf{L_{ef}}$ for the Stokes emission through the Raman active medium. Threshold intracavity pump intensity of 25 kW/cm^2 was reported for SRS in 12-μm diameter carbon disulfide droplets with Q of 10^8 at the Raman wavelength and an effective path length of L_{ef} ~5 m.[24] Let us compare this case with the conditions of our TERS experiments. The effective optical path length in microdroplets is defined as the optical distance traveled by the light circulating around the droplet circumference until the internal intensity decays to e-π and can be shown to be L_{ef} ≈ λQ /2πn, where λ is the vacuum wavelength and n is the droplet refractive index.[25] To make comparison with our case easier we first convert this value to L_{ef} defined at e^{-1} intensity decay, which is more natural in Fabry-Perot cavities. This conversion gives L_{ef} = 5 m/π ≈ 1.59 m. Due to the local near-field enhancement effect, the local pump intensity underneath the tip was ~1000 MW/cm2, that is 4x104 times higher than that achieved inside the droplets. We then assume ~10^3 enhancement in resonant Raman cross section and, therefore, in Raman gain as compared to that observed in spontaneous Raman scattering in highly transparent materials. At 4x104 times enhanced pump intensity and 10^3 times increased Raman gain, SRS threshold would be achieved for droplets with the effective path length of L_{ef} ≈ 1.59 m/4x10^7 ≈ 39.75 nm. From this simple estimate, we conclude that the effective path length L_{ef} required for SRS to occur is expected to reduce to nanometer scale under the excitation and resonant Raman enhancement conditions existing in our TERS experiments.

There might be another mechanism of enhancement in our case that is much more difficult to quantify. A rather large far-field-limited area of the laser focus is a source of scattered spontaneous Raman emission. Due to the described feedback mechanism that includes plasmonic tip enhancement, significant part of that spontaneous Raman emission

could find its way to the area under the tip apex with the very large Raman gain where it would contribute to SRS. This mechanism is not much different from deliberately injecting Stokes photons together with pump light in stimulated Raman spectroscopy,[3] where the rate of Stokes beam growth is proportional to the number of Stokes photons already present in the active medium. This additional enhancement mechanism could further reduce the estimated required value of L_{ef} to bring it even more closer to the actual value of that parameter in our TERS experiments, estimated as $2h_{NF} \approx 4$ nm.

4. SUMMARY AND CONCLUSION

In conclusion, we can conclude that Raman spectroscopy is a useful tool to characterize the pixel sidewalls. The application of a shorter-wavelength laser (near UV, e.g. 363.8 nm) will further decrease the laser spot (improved lateral resolution) and increase surface sensitivity due to shorter penetration depth. The decrease in Raman intensity due to smaller interaction volume for Raman scattering can be compensated by ω^4 factor in scattering intensity. An objective with higher NA (0.85-0.95) will increase the Raman signal collection and spatial resolution. One of our main goals is to simplify optical imaging and Raman spectroscopy on the nanoscale (single molecular scale) and make it affordable and user-friendly to most of AFM customers. Actoprobe R&D is focused on the development of a special AFM probe, AFM Active Optical Probe (AAOP), that combines a diode laser and a photodetector with an AFM probe as a monolithic device.[26, 27] The device integrates a tunable Raman laser and a tunable Raman detector on an AFM cantilever. It will dramatically improve the data quality for Tip Enhanced Raman spectroscopy (TERS) and microscopy. The AAOP will facilitate TERS and Raman imaging with nanometer resolution with as little complexity as conventional AFM imaging. Our team considers quantum dot and quantum dash-based laser materials to be good candidates for this optoelectronic device because of their unique optoelectronic properties. In particular, the broad gain spectrum of QD[28] and Q-dash[29] lasers allows tuning over 300 nm spectral range and fabricating diode laser with peak gain between 1 μm and 2 μm.[30] The small carrier-induced refractive index change[31] and low jitter[32, 33] are important for pulse applications of AAOP.

In TERS all applications for Research, we report on stimulated Raman scattering observed in a standard tip-enhanced Raman spectroscopy (TERS) experiment on a GaSb sample excited by 637-nm pump laser light. We explain our results by TERS-inherent mechanisms of enormous local field enhancement and by the special design and geometry of the ultra-high-aspect-ratio tips that enabled conditions for stimulated Raman scattering in the sample with greatly enhanced resonance Raman gain when aided by a microcavity to provide feedback mechanism for the Raman emission. The approach has great potential for further, orders-of-magnitude, progress in TERS enhancement by significantly increasing its nonlinear component we believe to have observed the phenomenon of stimulated Raman scattering in a standard AFM-based TERS experiment with only CW pump laser and with no special synchronous detection needed. We explain these observations by TERS-inherent mechanisms of enormous local field enhancement and by a special design and geometry of the UHAR tip that enabled conditions for SRS. We believe the TERS enhancement mechanisms could lead to tip-enhanced stimulated Raman scattering (TE-SRS) in the sample with greatly enhanced resonant Raman gain when aided by a microcavity to provide feedback mechanism for the Raman emission. The observed effect could be significantly enhanced by purposeful design of the tip. For example, the reflective surface can be enlarged with its curvature radius made equal to 11 or slightly less than the length of the tip to improve the scattered Raman light collection and its focusing to the tip, close to the tip apex area. The approach has great potential
for further, orders-of-magnitude, progress in TERS enhancement by significantly increasing its nonlinear component. We point out that the stronger the nonlinear effect, the shorter the required interaction length, and resonant absorption is not prohibitive if the required interaction length is much shorter than the penetration depth for the incident pump light and the backscattering scheme is used for collection of the scattered Raman light.

5. ACKNOWLEDGEMENT

This work was supported by SBIR US Army RDECOM CERDEC Night Vision and Electronic Sensors Directorate Contract W909MY-13-C-0011. This work was performed, in part, at the Center for Integrated Nanotechnologies, an Office of Science User Facility operated for the U.S. Department of Energy (DOE) Office of Science by Los Alamos National Laboratory (Contract DE-AC52-06NA25396) and Sandia National Laboratories (Contract DE-NA-0003525). The authors thank Dr. Elena Plis and Dr. Sanjay Krishna, Skinfrared LLC for providing FPA samples[34] for our TERS

experiments. The authors also acknowledge the faculty and technical staff of the Center for High Technology Materials at the University of New Mexico for fruitful conversations and technical support.

REFERENCES

[1] T. Deckert-Gaudig, A. Taguchi, S. Kawata *et al.*, "Tip-enhanced Raman spectroscopy – from early developments to recent advances," Chemical Society Reviews, 46(13), 4077-4110 (2017).

[2] R. C. Prince, R. R. Frontiera, and E. O. Potma, "Stimulated Raman Scattering: From Bulk to Nano," Chemical Reviews, 117(7), 5070-5094 (2017).

[3] H. K. Wickramasinghe, M. Chaigneau, R. Yasukuni *et al.*, "Billion-Fold Increase in Tip-Enhanced Raman Signal," ACS Nano, 8(4), 3421-3426 (2014).

[4] R. Zhang, Y. Zhang, Z. C. Dong *et al.*, "Chemical mapping of a single molecule by plasmon-enhanced Raman scattering," Nature, 498, 82 (2013).

[5] S. Jiang, Y. Zhang, R. Zhang *et al.*, "Distinguishing adjacent molecules on a surface using plasmon-enhanced Raman scattering," Nature Nanotechnology, 10, 865 (2015).

[6] Y. Zhilin, A. Javier, and X. Hongxing, "Electromagnetic field enhancement in TERS configurations," Journal of Raman Spectroscopy, 40(10), 1343-1348 (2009).

[7] J. K. Gimzewski, B. Reihl, J. H. Coombs *et al.*, "Photon emission with the scanning tunneling microscope," Zeitschrift für Physik B Condensed Matter, 72(4), 497-501 (1988).

[8] B. Pettinger, K. F. Domke, D. Zhang *et al.*, "Tip-enhanced Raman scattering: Influence of the tip-surface geometry on optical resonance and enhancement," Surface Science, 603(10), 1335-1341 (2009).

[9] C. Zhang, B. Gao, L. G. Chen *et al.*, "Fabrication of silver tips for scanning tunneling microscope induced luminescence," Review of Scientific Instruments, 82(8), 083101 (2011).

[10] Y. Uehara, Y. Suda, S. Ushioda *et al.*, "Tip shape dependence of the light emission efficiency for the scanning tunneling microscope," Applied Physics Letters, 79(11), 1718-1720 (2001).

[11] Z. C. Dong, X. L. Zhang, H. Y. Gao *et al.*, "Generation of molecular hot electroluminescence by resonant nanocavity plasmons," Nature Photonics, 4, 50 (2009).

[12] Y. Martin, and H. K. Wickramasinghe, "Method for imaging sidewalls by atomic force microscopy," Applied Physics Letters, 64(19), 2498-2500 (1994).

[13] J. H. Jang, W. Zhao, J. W. Bae *et al.*, "Direct measurement of nanoscale sidewall roughness of optical waveguides using an atomic force microscope," Applied Physics Letters, 83(20), 4116-4118 (2003).

[14] G. A. S. Alexander A Ukhanov, "Atomic force microscopy active optical probe," US Patent, 9482691 (2016).

[15] A. Partovi, D. Peale, M. Wuttig *et al.*, "High-power laser light source for near-field optics and its application to high-density optical data storage," Applied Physics Letters, 75(11), 1515-1517 (1999).

[16] C. C. Neacsu, S. Berweger, and M. B. Raschke, "Tip-Enhanced Raman Imaging and Nanospectroscopy: Sensitivity, Symmetry, and Selection Rules," NanoBiotechnology, 3(3), 172-196 (2007).

[17] B. Pettinger, P. Schambach, C. J. Villagómez *et al.*, "Tip-Enhanced Raman Spectroscopy: Near-Fields Acting on a Few Molecules," Annual Review of Physical Chemistry, 63(1), 379-399 (2012).

[18] N. Kumar, A. Rae, and D. Roy, "Accurate measurement of enhancement factor in tip-enhanced Raman spectroscopy through elimination of far-field artefacts," Applied Physics Letters, 104(12), 123106 (2014).

[19] L. Sirleto, A. Vergara, and M. A. Ferrara, “Advances in stimulated Raman scattering in nanostructures,” Advances in Optics and Photonics, 9(1), 169-217 (2017).
[20] H. M. Pask, “The design and operation of solid-state Raman lasers,” Progress in Quantum Electronics, 27(1), 3-56 (2003).
[21] D. C. Hamilton, “Resonant Raman Scattering from LO Phonons in Polar Semiconductors,” Physical Review, 188(3), 1221-1224 (1969).
[22] J. F. Scott, R. C. C. Leite, and T. C. Damen, “Resonant Raman Effect in Semiconductors,” Physical Review, 188(3), 1285-1290 (1969).
[23] R. M. Martin, and T. C. Damen, “Breakdown of Selection Rules in Resonance Raman Scattering,” Physical Review Letters, 26(2), 86-88 (1971).
[24] H. B. Lin, and A. J. Campillo, “Microcavity enhanced Raman gain,” Optics Communications, 133(1), 287-292 (1997).
[25] R. Symes, R. M. Sayer, and J. P. Reid, “Cavity enhanced droplet spectroscopy: Principles, perspectives and prospects,” Physical Chemistry Chemical Physics, 6(3), 474-487 (2004).
[26] T. J. R. T. Busani, P. Rathi, F. Jaeckel, and Alexander A. Ukhanov, Army SBIR phase I final report (2014).
[27] T. J. R. T. Busani, P. Rathi, F. Jaeckel, and Alexander A. Ukhanov, Army SBIR phase I option final report, (2015).
[28] A. A. Ukhanov, “PhD dissertation,” University of New Mexico, (2007).
[29] T. J. Rotter, “Ph.D. Dissertation,” University of New Mexico, (2007).
[30] G. Balakrishnan, S. Huang, T. J. Rotter *et al.*, “2.0 µm wavelength InAs quantum dashes grown on a GaAs substrate using a metamorphic buffer layer,” Applied Physics Letters, 84(12), 2058-2060 (2004).
[31] A. A. Ukhanov, A. Stintz, P. G. Eliseev *et al.*, “Comparison of the carrier induced refractive index, gain, and linewidth enhancement factor in quantum dot and quantum well lasers,” Applied Physics Letters, 84(7), 1058-1060 (2004).
[32] S. Hui, and F. L. Luke, “Dynamic properties of quantum dot distributed feedback lasers: high speed, linewidth and chirp,” Journal of Physics D: Applied Physics, 38(13), 2112 (2005).
[33] H. Su, “Ph.D. Dissertation,” University of New Mexico, (2004).
[34] T. J. Rotter, T. Busani, P. Rathi *et al.*, "Confocal Raman spectroscopy and AFM for evaluation of sidewalls in type II superlattice FPAs." 9451, 12.